Engineering Fracture Mechanics 260 (2022) 108167

Contents lists available at ScienceDirect

Engineering Fracture Mechanics

journal homepage: www.elsevier.com/locate/engfracmech

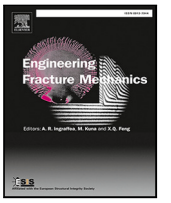

# Development of a microstructural cohesive zone model for intergranular hydrogen environmentally assisted cracking

Unai De Francisco *, Nicolas O. Larrosa, Matthew J. Peel

*Department of Mechanical Engineering, University of Bristol, UK*

ARTICLE INFO

*Keywords:*
Aluminium alloys
Hydrogen environmentally assisted cracking
Microstructurally short cracking
Cohesive zone model

ABSTRACT

During the initial stages of hydrogen environmentally assisted cracking (HEAC), including crack incubation, initiation and microstructurally short cracking, the geometrical configuration of the microstructure greatly influences the crack growth behaviour. Therefore, there is a big incentive to generate a model which can replicate intergranular HEAC at a microstructural scale. This report provides a general framework to implement a microstructural intergranular HEAC model by using a cohesive zone approach in Abaqus. The parameters of the phenomenological model were fitted by using in-situ synchrotron tomography observations of crack initiation and propagation during HEAC of AA7449-T7651. After fitting the parameters, the real HEAC behaviour of the aluminium alloy 7449-T7651 has been replicated accurately. Several characteristic HEAC features were achieved, including crack segmentation, preferential cracking along grain boundaries with a high resolved normal stress and cracks slowing down at grain boundary triple junctions. Comparisons with experimental observations show the suitability of this approach for the prognosis of crack initiation and propagation at a microstructural scale under HEAC conditions.

## 1. Introduction

Absorbed hydrogen can severely degrade the fracture resistance of high-strength alloys such as steel [1], titanium [2] and aluminium alloys [3,4]. Hydrogen environmentally assisted cracking (HEAC) involves the synergistic action of mechanical stresses and surface chemical reactions [4]. For specific material–environment combinations, chemical reactions at the alloy surface produce atomic hydrogen which can be subsequently absorbed into the alloy matrix. Consequently, critical concentrations of atomic hydrogen can lead to subcritical crack growth at stress levels significantly below yield. This compromises the structural integrity of many alloys used for a broad range of engineering components. Many investigations have been performed to understand the hydrogen embrittlement mechanisms which degrade the fracture resistance of different alloys. This has led to the postulation of several mechanisms. The most popular mechanisms include: hydrogen enhanced decohesion (HEDE) [5], hydrogen enhanced localised plasticity (HELP) [6] and the adsorption-induced dislocation emission (AIDE) mechanism [7].

Despite extensive research, the hydrogen accumulation, transport processes and hydrogen embrittlement mechanisms occurring during HEAC are not well understood. This can be ascribed to the difficulty of detecting the concentration and distribution of hydrogen within alloys. Several methods exist to measure the absorbed hydrogen content in metals [8–10]. However, it is not currently possible to measure the hydrogen content at a high enough resolution via non-destructive techniques to be able to understand the interaction of hydrogen with alloys during HEAC. Due to the limited understanding of the role of hydrogen during HEAC, there are no generic approaches for predicting the HEAC behaviour of alloys for specific material–environment combinations.

* Corresponding author.
*E-mail address:* ud13050@bristol.ac.uk (U. De Francisco).

https://doi.org/10.1016/j.engfracmech.2021.108167
Received 9 August 2021; Received in revised form 2 December 2021; Accepted 3 December 2021
Available online 22 December 2021

Finite element models can be useful to perform coupled hydrogen diffusion and stress analyses. Therefore, modelling has become an attractive approach of analysing the hydrogen embrittlement and HEAC behaviour of alloys [11–13].

The HEAC lifetime of components can be described by: crack nucleation at locations with critical hydrogen concentrations; growth of microstructurally short cracks; sustained crack propagation and fracture [14]. The lifetime of components is mainly dependent on the initial stages of HEAC, namely crack initiation and microstructurally short cracking. During these stages, the microstructural configuration relative to the sample/component geometry greatly influences the crack growth behaviour and rate [15]. For example, intergranular cracking in rolled plate materials is known to occur faster when the mode I tensile loading axis is aligned with the short transverse axis [3]. This can be ascribed to the greater resolved tensile stress normal to the grain boundaries.

Many experiments attempt to correlate changes in the HEAC sensitivity of alloys with different microstructural factors; such as the size, quantity and distribution of strengthening precipitates, the size of the precipitate free zone, the chemical composition of precipitates and the alloy matrix [16], and the grain size [17,18], shape and orientation relative to the loading axis and sample orientation. However, it is difficult to alter the material processing stages (such as the ageing treatment or the cold/hot work hardening treatment) of the alloys to vary only one of the material parameters. Therefore, the influence of other microstructure variables which cannot be perfectly controlled can overshadow the effect of the independent variable on the HEAC behaviour of the alloy [17]. Finite element microstructural modelling provides the capability of varying the grain size, shape and distribution without changing any other variables. Thus, the effect of these parameters which are critical during the initial cracking stages can be investigated in detail [19]. Additionally, microstructural models can be useful to predict the crack path and behaviour in different materials, such as polycrystalline alloys [20,21] and particle reinforced composites [22,23].

Several approaches have been used to model the hydrogen embrittlement and HEAC behaviour of various alloys at different length scales including: the phase field fracture method [24], strain gradient plasticity-based models [12], atomistic simulations [25] and ductile damage models [26]. Another common approach is the use of cohesive zone models [27–31]. In these phenomenological models, cracking occurs along predefined interface cohesive elements/surfaces. The main advantage of the cohesive zone approach is that it can account for both crack initiation and crack propagation [32]. Furthermore, as cohesive models are phenomenological in nature, the cohesive parameters can be adjusted to match the failure behaviour of the material under investigation without explicitly representing a specific crack growth mechanism [31]. The cohesive law for interface damage is usually developed on the basis of the microstructure. An example is the cohesive law for fibre reinforced composites (e.g. the cohesive law for helical fibres [33]).

Simonovski and Cizelj investigated the use of a cohesive zone model for intergranular microstructural environmentally assisted cracking [34]. A microstructural mesh with cohesive elements at the grain boundaries was generated from the tomography data of a stainless steel wire. By applying a time-dependent degradation on the cohesive elements, intergranular cracking was achieved. This investigation aims to build on this research by Simonovski and Cizelj [34–36] by incorporating a coupled mass-diffusion stress analysis to apply a hydrogen-dependent rather than a time-dependent degradation on the cohesive surfaces. Additionally, this investigation aims to recreate the real HEAC behaviour observed in aluminium alloys to assess the suitability of these models for crack prognosis. Finally, the use of adjustable synthetic 3-dimensional microstructures is investigated to analyse the variability in the crack growth rates by performing Monte Carlo simulations.

### *1.1. Aims and scope*

The primary aim of this work is to provide a general framework to model intergranular HEAC at a microstructural scale in 3D by using a coupled diffusion stress analysis in Abaqus. Such a model can be a powerful tool to analyse the influence of the grain size, shape and distribution on the HEAC behaviour. Additionally, the model can provide a framework to predict the HEAC behaviour of alloys for more complex sample geometries and loading conditions. Further, the simultaneous collection of data for the transport of hydrogen and the evolution of cracks can be used to better understand the mechanical and chemical processes involved during HEAC by systematically varying the constitutive equations for the material mechanical and diffusion equations as well as the boundary conditions.

This report provides a detailed description of the methodology used to implement a microstructural intergranular HEAC model in Abaqus. The HEAC behaviour of 7xxx aluminium alloys has been used as a case study to exemplify the implementation of the model. In this case, the parameters of the model were calibrated to reproduce the HEAC behaviour observed for the aluminium alloy 7449-T7651 during an in-situ tomography experiment. The structure of this article can be divided into four main sections:

i. A description of the case study: intergranular HEAC of 7xxx aluminium alloys. This section contains an outline of the experimental methods and results for the reference experiment for the HEAC behaviour of AA7449-T7651.
ii. The methodology used to implement the model and the constitutive relations defining the mechanical and diffusion behaviour of the grains (solid elements) and the grain boundaries (cohesive surfaces).
iii. A results section comparing the HEAC behaviour observed in the model and experimentally.
iv. A discussion section, examining the main limitations of the model.

**Table 1**
The values used for the synthetic microstructure parameters in Dream.3D. The parameters $\mu$, $min$ and $max$ are given for an ESD in μm.

| $\mu$ | $\sigma$ | Bin size (μm) | $min$ | $max$ | $A/B$ | $A/C$ |
|---|---|---|---|---|---|---|
| 5.3 | 0.3 | 30 | 3 | 1 | 50 | 500/3 |

## 2. Case study

7xxx aluminium alloys are sensitive to HEAC when subjected to static tensile loading in moist air environments and aqueous solutions [3,15,37]. Small scale observations of crack initiation and growth provide a useful reference to build microstructural finite element HEAC models. A previous investigation by the authors involved monitoring the HEAC behaviour of the novel alloy AA7449-T7651 in a moist air environment using in-situ 3D microtomography observations. This investigation aims to replicate the HEAC behaviour observed from this experiment by using a cohesive zone model. This section briefly describes the experimental methods and results of the in-situ HEAC tomography investigation. A detailed description of the methods and findings from this experiment can be found in a previous article by the authors [38].

Two samples of aluminium alloy 7449-T7651 with a 1 mm diameter gauge section were statically loaded in tension to an initial stress of 141 and 184 MPa (28 and 37% of yield stress). Subsequently, the samples were exposed to an environment with a high temperature and relative humidity of 76 °C and 73% respectively. This enabled HEAC to occur rapidly, such that the uncracked samples of AA7449-T7651 fractured completely within an exposure time of 240 min. During HEAC, the samples were imaged iteratively using synchrotron X-ray microtomography. A fast imaging time of approximately 8 min per tomogram, allowed taking multiple snapshots during the HEAC process, capturing both crack initiation and propagation.

Initial HEAC was exclusively brittle intergranular. After prolonged exposure, large surface cracks in close proximity to each other coalesced. The coalescence of cracks led to a decrease in the effective cross sectional area of the samples, resulting in rapid overload.

## 3. Intergranular HEAC cohesive zone model

This section describes the cohesive zone model used to recreate intergranular HEAC at a microstructural scale, including:

i. how to produce a representative synthetic microstructure,
ii. how to perform a coupled stress and diffusion analysis in Abaqus,
iii. defining the constitutive mechanical and hydrogen diffusion behaviour of the grains (solid elements) and the grain boundaries (cohesive surfaces).

### 3.1. Microstructure

The microstructure was modelled using the software Dream.3D [39]. The generation variables are summarised in Table 1. The distribution is specified by the average $\mu$ and standard deviation $\sigma$ of the lognormal grain size as equivalent sphere diameter, ESD [40]. The size of the grains was truncated to avoid small grains, which are computationally complex, and very large grains, that lead to unrepresentative local microstructures i.e.

$$e^{(\mu-\min\cdot\sigma)} < ESD < e^{(\mu+\max\cdot\sigma)}. \tag{1}$$

Additionally, the ratios $A/B$ and $A/C$ represent the average aspect ratios of the grains, where $A$, $B$ and $C$ are the average lengths along the longitudinal, transverse and short transverse direction, respectively.

An example of a synthetic microstructure generated using the parameters in Table 1 is compared with the real microstructure of AA7449-T78651 in Fig. 1. Dream.3D generates a cuboidal synthetic volume composed of cubic elements for the given grain size statistics; where each cubic element is labelled as belonging to a specific grain. More complex sample geometries require a mask to eliminate the elements from the cubic volume which are not enclosed by the sample geometry. The synthetic microstructure then needs to be processed to generate a suitable mesh for Abaqus. Firstly, the grains within the volume are exported as independent STL files with a triangular surface mesh. Subsequently, the software GMSH uses the STL files to generate a 3D mesh with tetrahedral elements for each grain, and exports the mesh as a readable input file for Abaqus [41]. MATLAB code was developed to process the input file to: (a) assign material properties to the grains, (b) define the cohesive surfaces at the grain boundaries, (c) assign properties to the cohesive surfaces and (d) apply the boundary and loading conditions.

### 3.2. Coupled diffusion-stress analysis

The model requires a coupled mass diffusion-stress analysis, in order to model the transport of hydrogen and the cracking behaviour within the aluminium alloys simultaneously. However, a coupled mass diffusion-stress analysis is not available in Abaqus. To overcome this issue, previous hydrogen embrittlement and HEAC models in Abaqus have been implemented using a coupled thermal-stress analysis [28,31,42,43]. This exploits the analogous structure between Fourier's thermal conductivity equation and the diffusion equation, by co-opting the nodal temperature as the hydrogen concentration [28,42,43]. Thus, to enable a coupled mass diffusion-stress analysis, C3D4T elements (4-node thermally coupled tetrahedron with linear displacement and temperature) from the Abaqus element library were used for the grains.

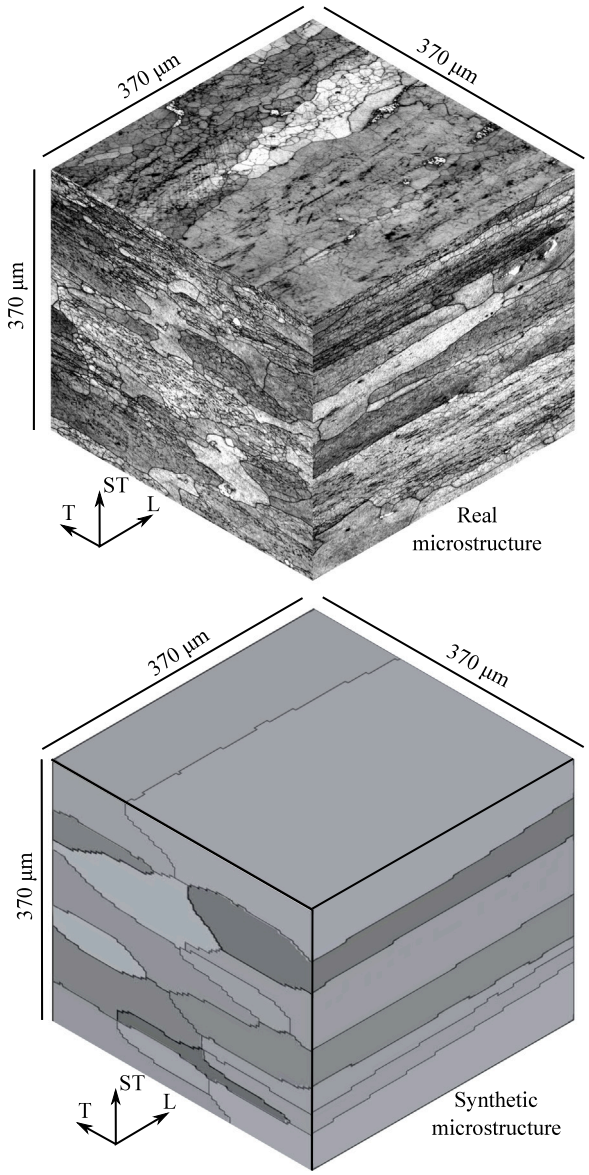


**Fig. 1.** (a) The microstructure of AA7449-T7651 along three different planes after etching with Weck's reagent. (b) A synthetic microstructure generated using Dream.3D, approximating that of AA7449-T7651. T, ST and L represent the transverse, short transverse and longitudinal axes respectively.

### *3.3. Constitutive behaviour*

This section describes the three main parts defining the constitutive behaviour of the material, including:

i. the mechanical behaviour of the material within the grains,
ii. the internal hydrogen mass-diffusion behaviour within the grains,
iii. the mechanical and diffusion behaviour at the grain boundaries (cohesive surfaces).

#### *3.3.1. Material behaviour*

The samples were tested well below the yield stress of the material, so the mechanical response of the grains was modelled following linear elasticity. Additionally, the material can be assumed to be isotropic with a Young's modulus ($E$) and Poisson's ratio ($\nu$) of 71 GPa and 0.33 respectively, due to the similarity with AA7075 [44].

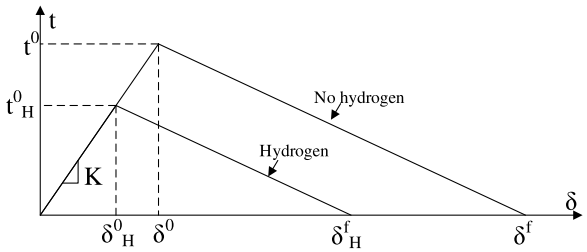


**Fig. 2.** The traction–separation response with linear softening for cohesive surfaces. The influence of hydrogen on the T–S response is exemplified.

### 3.3.2. Hydrogen diffusion

The hydrogen diffusion behaviour was modelled following the equation [28]

$$\frac{\delta C_L}{\delta t} - \nabla \cdot (D_L \nabla C_L) = 0. \tag{2}$$

where $C_L$ is the concentration of free hydrogen at interstitial lattice sites, $t$ represents time and $D_L$ is the mass diffusivity of interstitial hydrogen. This neglects the effect of the hydrostatic stress gradient and plasticity, which is reasonable at the early stages of cracking, and also hydrogen trapping sites such as vacancies. From Eq. (2), the only parameter that must be defined to model the diffusion behaviour is the diffusivity, $D_L$. This parameter typically follows the equation [45]

$$D_L = D_0 \exp -\frac{E_A}{RT}, \tag{3}$$

where $D_0$ is a pre-exponential coefficient, $E_A$ is the activation energy, $R$ is the ideal gas constant and $T$ is the absolute temperature.

### 3.3.3. Cohesive surfaces (UINTER)

Cohesive *elements* with a geometric thickness are well suited to modelling along a predefined fracture plane (e.g. debonding of an adhesive layer). During intergranular HEAC, cracking may occur along any high angle grain boundary and generating a mesh with cohesive elements along all valid adjacent grain boundaries is difficult. Instead, cohesive *surfaces* can be used, where the constitutive traction–separation (T–S) response is implemented by defining the surface interaction behaviour of the interface. The T–S response of a cohesive surface typically involves linear-elastic deformation, damage evolution and fracture. When the cohesive surface meets the fracture criterion, the traction drops to zero and follows a hard contact pressure–overclosure relationship [46].

A linear softening traction–separation response was used, as illustrated in Fig. 2. Initially, the traction increases linear-elastically with displacement, following the relationship

$$\begin{pmatrix} \bar{t_n} \\ \bar{t_s} \\ \bar{t_t} \end{pmatrix} = \begin{bmatrix} K_{nn} & 0 & 0 \\ 0 & K_{ss} & 0 \\ 0 & 0 & K_{tt} \end{bmatrix} \begin{pmatrix} \delta_n \\ \delta_s \\ \delta_t \end{pmatrix}, \tag{4}$$

where $\bar{t}$ is the elastic traction, $K$ is the stiffness, $\delta$ is the separation, the subscript $n$ represents the normal direction and the subscripts $s$ and $t$ represent the shear directions. In the case of HEAC of 7xxx alloys, crack growth at the grain boundaries is primarily dependent on the resolved tensile stress normal to the grain boundary [15]. Therefore, the damage initiation and fracture criteria were based on the traction and displacement along the normal direction ($t_n$ and $\delta_n$). The onset of damage was defined using the maximum stress criterion, i.e. as the normal traction $t_n$ reaches a maximum value $t^0$. Beyond this point, the cohesive surface starts accumulating damage and enters the linear-softening stage. The traction along the normal direction, $t_n$, can then be updated following the relationship

$$t_n = \bar{t_n}(1 - D), \tag{5}$$

where $D$ is a damage variable, calculated as

$$D(\delta_n) = \begin{Bmatrix} 0 & ; & \delta_n \le \delta^0 \\ \frac{\delta^f(\delta_n - \delta^0)}{\delta_n(\delta^f - \delta^0)} & ; & \delta_n > \delta^0 \end{Bmatrix} \tag{6}$$

where $\delta^0$ is the displacement at the onset of damage ($\bar{t_n} = t^0$) and $\delta^f$ is the displacement at fracture.

To model the hydrogen damage, it was assumed that the main hydrogen embrittlement mechanism affecting 7xxx alloys is the HEDE mechanism. The HEDE mechanism associates hydrogen embrittlement with a reduction in the cohesive strength of grain boundaries or other interfaces caused by the accumulation of segregated atomic hydrogen [47]. To apply a hydrogen-affected reduction in the cohesive strength, the traction–separation curve was varied as a function of the local hydrogen concentration. In the case of 7xxx alloys, the influence of hydrogen on the cohesive strength of the grain boundaries is not well understood. Therefore to facilitate fitting, the most simplistic approach was used, where $t^0$ (damage initiation traction) and $\delta^f$ (separation at fracture) decrease linearly with the local hydrogen concentration (Fig. 2). This can be expressed as

$$t^0_H = t^0 \cdot (1 - \phi \cdot C_L), \tag{7}$$

and

$$\delta_H^f = t^0 \cdot (1 - \phi \cdot C_L), \tag{8}$$

where the subscript $H$ denotes adjusted variables to account for the local hydrogen concentration, $C_L$ is the local hydrogen concentration and $\phi$ is a softening parameter which is usually obtained by fitting [48]. This method of applying a linear hydrogen degradation has been previously used by several authors [48–50].

At the onset of damage, an elastic snap-back instability occurs leading to convergence issues [32]. To overcome this problem, Simonovski and Cizelj applied a small amount of viscous regularisation on the traction–separation law [36]. In this case, a viscous stiffness degradation parameter is used instead of $D$. The viscous stiffness degradation, $D_v$, is obtained via the equation [36]

$$\dot{D}_v = \frac{1}{\mu} \cdot (D - D_v), \tag{9}$$

where $\mu$ is the viscosity parameter and $\dot{D}_v$ is the rate of change of the viscous stiffness degradation. This type of viscous regularisation was incorporated to the model by updating the new degradation parameter (damage factor) using the equation

$$D_v^n = \frac{D^n \Delta t + D^{n-1} \Delta t + D_v^{n-1} \cdot (2\mu - \Delta t)}{\Delta t + 2\mu}, \tag{10}$$

where $\Delta t$ is the time increment for the step and the superscripts $n$ and $n-1$ denote the values for the current and previous step respectively.

## 4. Model implementation

This section describes the procedure used to implement the cohesive zone model for the case study. Firstly, a microstructural mesh was generated for the gauge section of a cylindrical tensile sample by using tetrahedral elements. The experimental conditions during the $\mu$CT tests were then simulated by subjecting the sample to a static displacement step, followed by an exposure step to initiate the ingress of hydrogen and cracking.

### 4.1. Mesh and cohesive surfaces

For the case study, the gauge volume of the sample was modelled as a 1 mm diameter and 0.5 mm tall cylinder. Therefore a cylindrical mask was used in Dream.3D to obtain the required sample geometry, as represented in Fig. 3(a). For the current simulation, a microstructural mesh was produced using the parameters in Table 1 with an average element size of 20 μm. Figs. 3(b) and (c) show the tetrahedral elements and cohesive surfaces for the microstructural mesh, respectively. The model contains a total of 153 grains and 803 grain boundaries. The element faces of adjacent grains match perfectly at the grain boundaries. Thus, the grain boundaries were defined by using the matching element faces of the grains at the interface.

### 4.2. Boundary conditions

The rate of damage is limited by the transportation of hydrogen to the fracture process zone. The hydrogen transport process, illustrated in Fig. 4, involves (1)–(2) the transport of the hydrogen-containing molecules ($H_2O$) to the surface, (2)–(3) the dissociation and absorption of $H^+$ ions into the alloy matrix, (3)–(4) hydrogen diffusion to the fracture process zone and (4) the fracture due to hydrogen embrittlement at weakened grain boundaries [51].

In order to simplify the HEAC model, it is necessary to understand which part of the process is the rate limiting step [52]. For example, if hydrogen is produced at the surface more quickly than it can diffuse within the sample, the hydrogen concentration at the sample surface can be fixed at saturation levels. Only the constitutive equations relating to the internal diffusion of hydrogen need to be considered. Conversely, if the surface generation of hydrogen is limited, the model can be simplified by assuming that hydrogen diffuses almost instantaneously via a suitably large value for the mass-diffusivity of hydrogen, $D_L$. In this case, the exposed surfaces cannot be considered to be at saturation levels and the mass-flux of hydrogen ($q$) at the exposed surfaces in the model must be accurately modelled.

The appropriate choice of boundary condition is readily informed by a comparison of experimental tomography data with two versions of the model: one with a surface-reaction limit and the other with a diffusion limit. This procedure was simulated in Abaqus by using the 153 grain microstructure from Fig. 3 and used conditions for the sample tested at 141 MPa. The process involved two steps, illustrated in Fig. 5:

i. Static displacement (ramp): The application of a displacement $\Delta Z$ of 0.4965 μm in the axial direction for the nodes at the top and bottom surfaces of the cylinder. This represents the displacement required to subject the sample to a tensile load of 141 MPa. The hydrogen concentration was set to zero, assuming no previous exposure.
ii. Moist air exposure (transient): This step was executed over a step time of 240 min i.e. the time to fracture in the experiment. Two conditions were used:
    (a) (Surface-limited): Set a constant hydrogen flux at the element faces of the external sample surface and, after the apparition of cracks, at the fractured surfaces.
    (b) (Diffusion-limited): Decrease the diffusivity and fix the hydrogen concentration at the nodes of the external sample surface and the fracture surfaces of cracks, representing saturation levels.

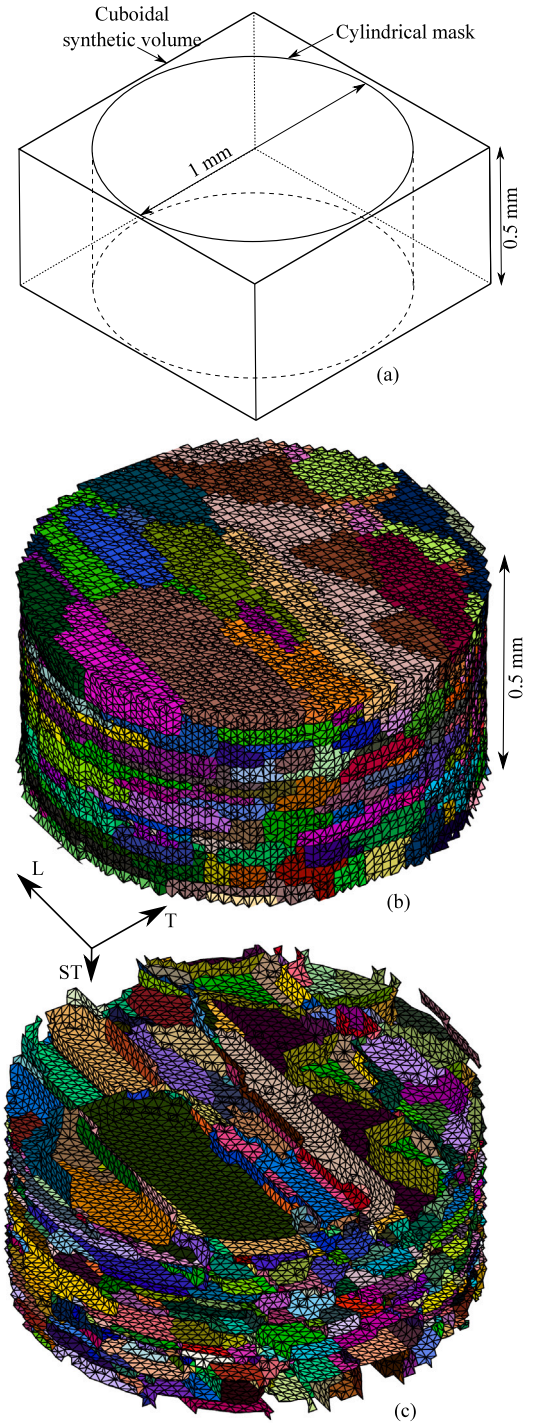


**Fig. 3.** The mesh for the gauge section of a cylindrical sample (1 mm diameter, 0.5 mm tall) with 153 grains. (a) Diagram exemplifying the use of a cylindrical mask to discard unnecessary elements from the cuboidal synthetic volume in Dream.3D. (b) The 3D mesh with tetrahedral elements for each grain. The average element size is 20 μm. (c) Triangular 2D mesh for each grain boundary (size also 20 μm).

## 5. Model calibration

In order to calibrate the model, the cracking behaviour under static loading conditions attempted to reproduce the tomography results both quantitatively and qualitatively. The HEAC behaviour was quantitatively calibrated by equating the output fractured

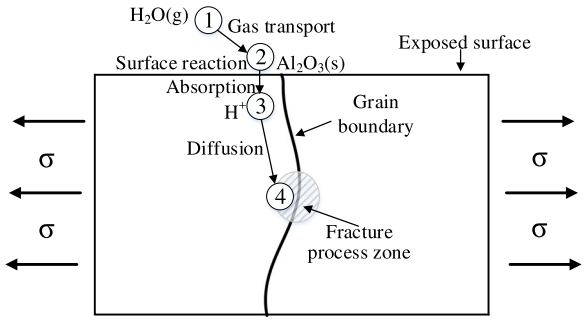


**Fig. 4.** Diagram illustrating the transport of hydrogen to the fracture process zone from a moist air environment.

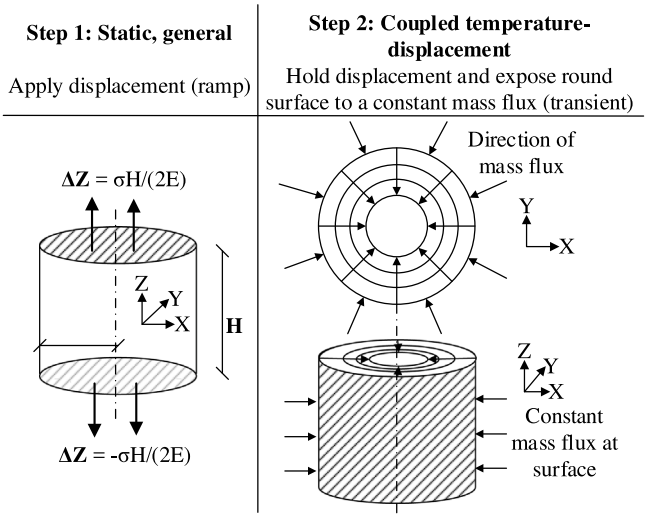


**Fig. 5.** Diagrams showing the loading and boundary conditions for the steps applied in Abaqus. The first step involves gradually loading the sample to the required displacement. For the second step, the sample is held at the same position and hydrogen is introduced at the exposed sample surface.

**Table 2**
The values used for the material properties of the grains and the traction–separation response parameters of the grain boundaries. $q$ and $C_L$ represent the hydrogen flux and the hydrogen concentration, respectively, at the sample surface and cracked surfaces.

| Material properties | | Reaction controlled | Diffusion controlled |
|---|---|---|---|
| $E$ | (GPa) | 71 | |
| $\nu$ | – | 0.33 | |
| $D_L$ | ($m^2$/s) | $2 \times 10^{-10}$ | $5 \times 10^{-13}$ |
| Cohesive T–S parameters | | | |
| $K_{nn}$ | (GPa/m) | 8.0 | |
| $K_{ss} = K_{tt}$ | (GPa/m) | $10^7$ | |
| $t^0$ | (KPa) | 4.2 | |
| $\delta^f$ | (mm) | $5.4 \times 10^{-4}$ | |
| $\phi$ | – | 0.0075 | |
| $\mu$ | – | 0.2 | |
| Boundary conditions | | | |
| $\Delta Z$ | (μm) | 0.4965 | |
| $q$ | – | $1.4 \times 10^{-6}$ | – |
| $C_L$ | – | – | 100 |

fraction over time. The fractured fraction represents the total sample area normal to the loading direction covered by the cross-sectional area of cracks as a fraction of the sample cross-sectional area. The evolution of the fractured fraction of the model was matched with the experimental results through trial an error, by iteratively varying the model cohesive T–S parameters. Fig. 6 shows examples of the fractured fraction of the surface-reaction controlled model for several trials used to analyse the influence of the

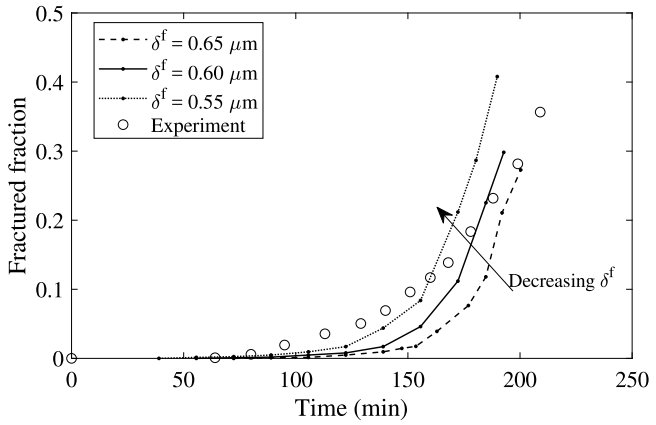


**Fig. 6.** The fractured fraction for the surface-reaction controlled model for varying values of $\delta^f$. The experimental values for the 141 MPa sample have also been included for comparison. $K_{nn}$ = 110 GPa/m, $t^0$ = 50 KPa, $\phi$ = 0.0085, $\mu$ = 0.2. All other parameters are the same as those in Table 2.

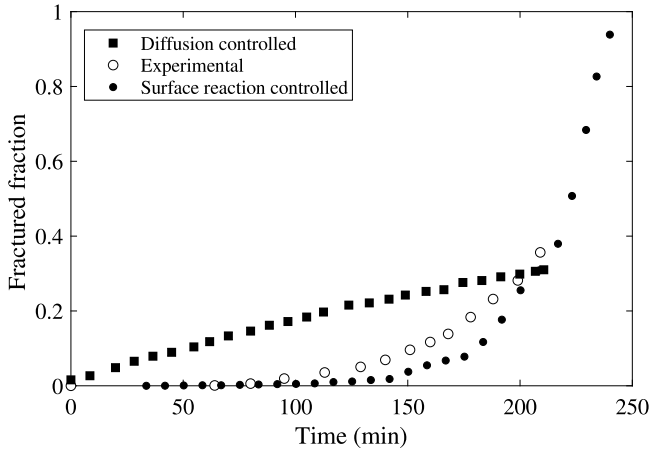


**Fig. 7.** Graph comparing the evolution of the cross-sectional area of the sample covered by cracks for the model with a synthetic microstructure and the experiment. A curve has also been added for a diffusion controlled case for comparison.

displacement at fracture for the cohesive surfaces ($\delta^f$). Decreasing the value of $\delta^f$ results in faster crack growth and fracture. After performing similar trials with other parameters ($K_{nn}$, $t^0$, $\phi$, $D_L$), the final values used for the surface-reaction and diffusion controlled models have been specified in Table 2. The relevant parameters for the interaction of hydrogen with the material include: $D_L$, $\phi$ and $q$. Due to the phenomenological character of the model, the surface hydrogen flux, $q$, was set to an arbitrary value (without units) and the hydrogen damage coefficient $\phi$ was calibrated accordingly.

## 6. Results

Fig. 7 compares the fractured fraction for the surface-limited and diffusion-limited models with the experimental values for the sample subjected to an initial stress of 141 MPa. For the surface-limited case, the rate of fracture follows an exponential curve similar to the experimental observations. Conversely, the cracking behaviour for the diffusion-limited model predicts crack growth rates that decrease with time. Diffusion control is modelled with an instantaneously high hydrogen concentration near the sample surface, resulting in rapid crack initiation, but subsequent hydrogen diffusion into the sample is limited by the local concentration gradients. As the total hydrogen concentration of the sample increases, the concentration gradients decrease, leading to a reduction in the hydrogen influx (Fig. 8). This, in turn, leads to a reduction of the crack growth rates with time. However, this decrease is not very pronounced as the lower hydrogen flux at the sample surface is countered by the extra hydrogen influx at new crack surfaces. In contrast, for the surface-reaction controlled case, the hydrogen influx at the sample surface remains constant over time ($t$ < 150 min in Fig. 8). Therefore, the additional hydrogen flux at cracked surfaces ($t$ > 150 min in Fig. 8) drive an acceleration in the fracture rate. Thus, it is much more likely that the HEAC rates for the tomography samples were limited by the surface-reaction rates.

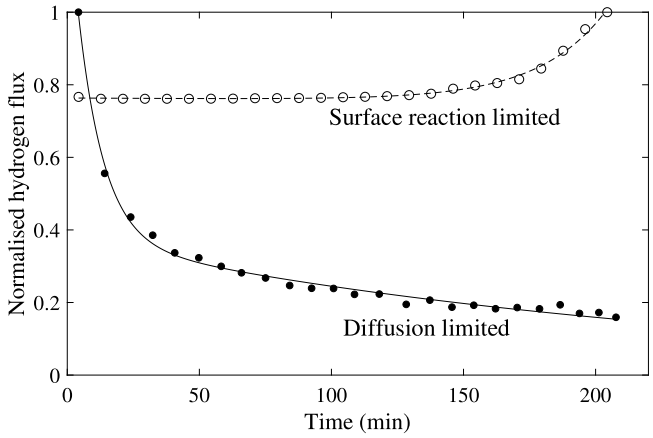


**Fig. 8.** The hydrogen flux over time for the diffusion controlled and the surface-reaction controlled models. The flux was calculated from the rate of change of the average hydrogen concentration in the samples. The hydrogen flux was normalised by dividing by the maximum value of the series.

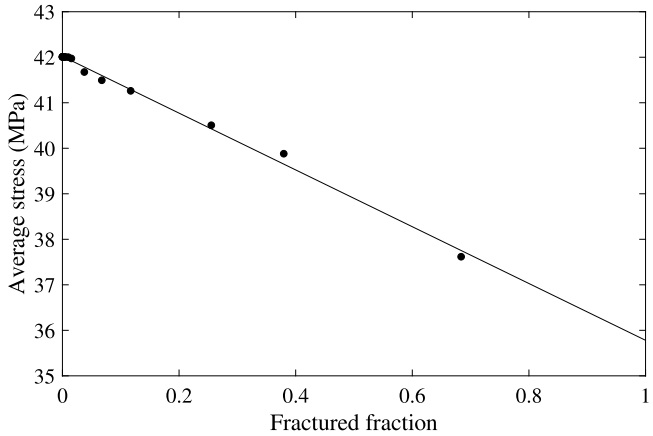


**Fig. 9.** The average von Mises stress of the bulk tetrahedral elements vs. the fractured fraction for the surface-reaction controlled model. A best fit line has been included, showing a linear decrease in the average stress with the fractured fraction.

The crack growth rates are also affected by other factors which are applicable to both boundary conditions. For example, crack growth is diminished by a reduction in the average stress with time, caused by crack propagation under constant displacement conditions (Fig. 9). Additionally, as cracks become larger, the crack mouth opening displacement increases, driving an acceleration in the fracture rate.

Fig. 10 shows a histogram of the von Mises stress at the centroid of each element after loading to the required displacement (no cracking or exposure). The average stress of the elements was approximately 42 MPa, considerably below the required stress of 141 MPa. This can be ascribed to the high compliance of the cohesive surfaces relative to the elastic modulus of the alloy, resulting in large displacements at the grain boundaries. Therefore, to further use the model to compare the influence of different microstructures on the HEAC behaviour, the stiffness of the cohesive surfaces needs to be increased. Otherwise, the nominal stress in the model is dependent on the amount of grain boundaries per unit volume, such that a model with a very large grain size would have a larger stress for an identical sample geometry.

Figs. 11 and 12 show 2D and 3D snapshots for the evolution of intergranular cracks in the surface-reaction controlled model, the diffusion controlled model and the tomography sample subjected to 141 MPa. For the snapshots of the model, the cracks are shown as the mesh of fractured cohesive surfaces. Qualitatively, the HEAC behaviour of the surface-reaction controlled model and the experiment appear to be comparable. Several similarities can be observed:

i. At the beginning, cracks only grow at grain boundaries which are orthogonal to the loading axis. This response was achieved in the model by limiting the damage evolution and fracture criteria to the normal displacement and traction at the cohesive surfaces.
ii. The sequential nucleation of separate intergranular cracks, primarily at or near the sample surface. Sequential crack nucleation indicates that specific grain boundaries were more prone to crack initiation. This can be influenced by the proximity of the grain boundary to the surface, the size of the grain boundary, the orientation of the boundary relative to the loading axis and

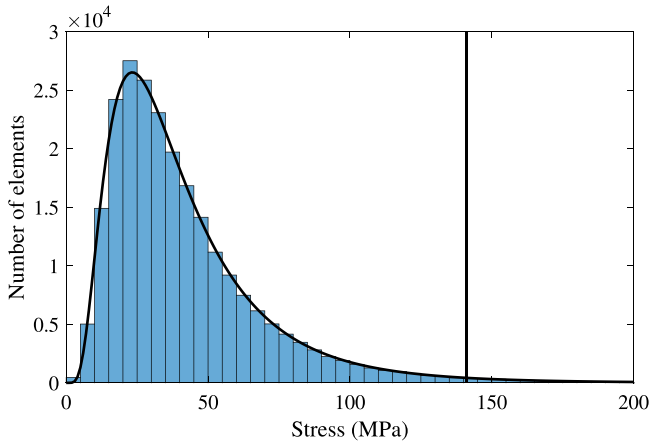


**Fig. 10.** Histogram showing the stress in the tetrahedral elements of the surface-reaction controlled model after the loading step (no exposure). A bin size of 2 MPa was used. The stress can be seen to follow a lognormal distribution. A lognormal fit with a mean and standard deviation of 3.54 and 0.626 has been overlaid (units in MPa). A vertical line has also been included at 141 MPa, denoting the required tensile stress. It can be seen that the stress of the majority of the elements in the model is significantly below the required stress.

the interaction of the grain boundary with the surrounding microstructure. Large grain boundaries near the sample surface are more sensitive as the displacement is greater due to the lack of constraint, due to both contributions. Further, the hydrogen concentration is greater at the sample surface than at the centre of the sample. However, due to the high diffusivity in the surface-reaction controlled model, this difference in the hydrogen concentration is negligible.

iii. The formation of crack clusters which do not coalesce due to the lack of coplanarity between cracks.

iv. The appearance of the largest crack occurring at a location of the sample surface which is tangential to the longitudinal axis (labelled as (1) and (i) in Fig. 12). This is because there are more broad grain boundaries with a large portion of the perimeter on the sample surface at locations where the rolling direction is tangential to the sample surface.

v. Some cracks may nucleate internally, rather than at the sample surface (examples in Fig. 15). The crack growth rate of these cracks is found to accelerate rapidly after surfacing due to a greater crack opening displacement.

In the model, many cracks were found to propagate along adjacent co-planar grain boundaries (cracks with multiple colours in Fig. 12). The crack labelled as (i) in Fig. 12 is highlighted in Fig. 13 as an example. Initially, the crack formed along a single grain boundary with a large normal displacement. After 134 min, the crack slowed down at the triple junction of the co-planar grain boundaries and had a skewed shape as a result. As the crack propagated past the triple junction, the maximum opening displacement increased rapidly due to the reduced constraint and lower traction at the interface, leading to rapid crack growth. This behaviour was consistent with the experimental observations from the tomography sample. An example has been presented in Fig. 14. Fig. 14(a) shows an SEM image of the fracture surface for the crack labelled as (1) in Fig. 12. Further, a graph showing the crack growth rate of crack (1) has been presented in Fig. 14(b). The graph shows that the crack growth rate momentarily decreases when the crack front approaches triple junctions.

Fig. 15 shows several close-up snapshots of the cracks labelled as (i), (ii) and (iii) in Fig. 12 within the surrounding microstructure. Crack (i) was the first large crack to form and can be seen to grow rapidly along two co-planar grain boundaries until it approaches two almost perpendicular grain boundaries at a '⊥'-shaped triple junction. Since the grain boundaries beyond this junction are not favourably aligned with the tensile axis, the crack slows down. As a consequence, a second crack (ii) nucleates at a nearby, large and favourably oriented boundary. This results in segmented crack growth, which is a characteristic feature of the HEAC behaviour of 7xxx alloys [15,53]. However, after prolonged crack growth, the ligaments which form in between crack segments typically yield and fracture [53]. In this case, the model does not account for this kind of crack coalescence, as fracture is limited to intergranular cracking at grain boundaries with a high resolved normal stress. However, the model can still reproduce intergranular crack coalescence of initially independent nearby cracks. For the experiment, crack coalescence caused the effective cross-sectional area of the sample to decrease, resulting in rapid overload after a fractured fraction of 40% was reached. In contrast, the cracks in the model did not cause complete fracture even after a fractured fraction of 90% was exceeded. Therefore, it is necessary to implement transgranular cracking in the model to more accurately simulate the fracture behaviour during final ductile overload.

From Fig. 12, the HEAC behaviour for the diffusion controlled model can be seen to differ considerably with respect to the experimental results and the surface-reaction controlled model. Due to the rapid increase in the hydrogen concentration at the surface, many cracks formed for the diffusion limited model after a short period of time. For example, after an exposure time of 80 min, 16 cracks had nucleated for the diffusion controlled model, but only 2 had nucleated for the tomography sample and 1 for the reaction controlled model. Additionally, the slower in-depth penetration of hydrogen for the diffusion controlled model resulted in cracks growing preferentially around the sample circumference. In contrast, for the experimental and surface-reaction controlled model, cracks were found to propagate both radially and around the sample surface. This provides further evidence that HEAC of the real samples was likely limited by the surface-reaction rate.

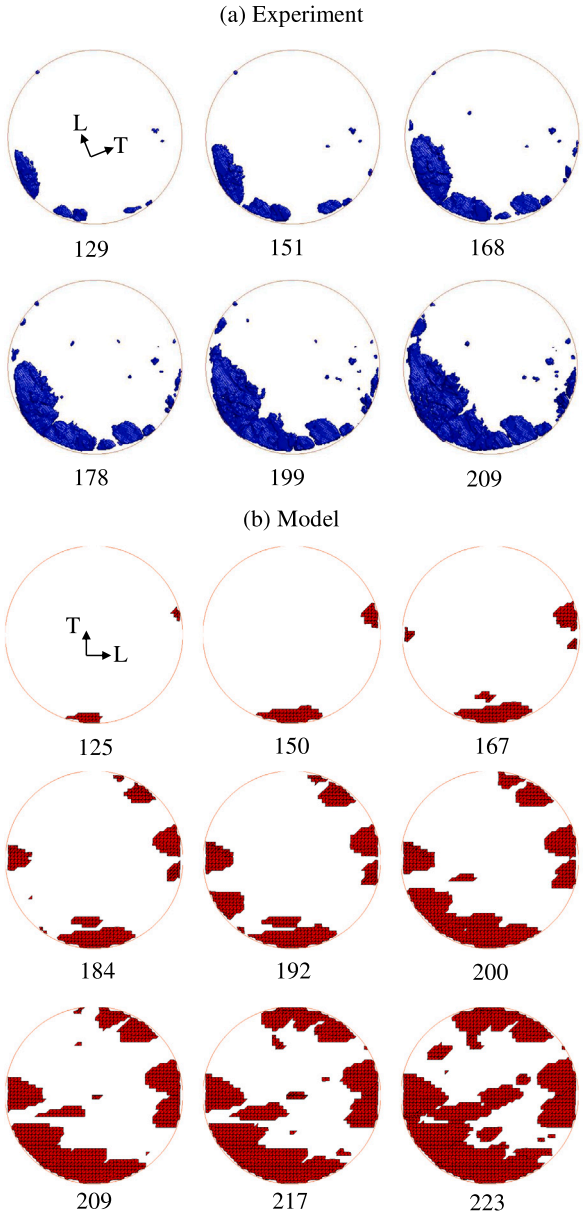


**Fig. 11.** The cross-sectional area of the samples covered by cracks over time (a) experimentally and (b) in the surface-reaction controlled model. The images show a projection onto the L–T plane of all of the cracks present. The circles denote the approximate location of the sample surface. Each snapshot has been labelled with the exposure time in minutes.

### *6.1. Impact of microstructure variability*

The grain size statistics in Table 1 were used to produce ten random synthetic microstructures in Dream.3D. Fig. 16 shows the evolution of the fractured fraction for each sample after following the same procedure (surface-reaction controlled). The fracture rates can vary significantly from sample to sample; despite using identical grain size statistics for the microstructure generation. For the sample in the experiment, ductile overload occurred after a fractured fraction of 40% was reached. For the simulations, the time required to reach a fractured fraction of 40% ranged between 193 and 232 min for the ten samples analysed. The mean and standard deviation were estimated as 211 and 13 min respectively. This is indicative of the high variance between each microstructure. Most of the curves have an exponential shape, similar to the experimental results. However, for several samples where cracking initiated early, the curves have an irregular shape. This is due to the fluctuating crack growth rates resulting from the surrounding microstructure of a single dominant crack.

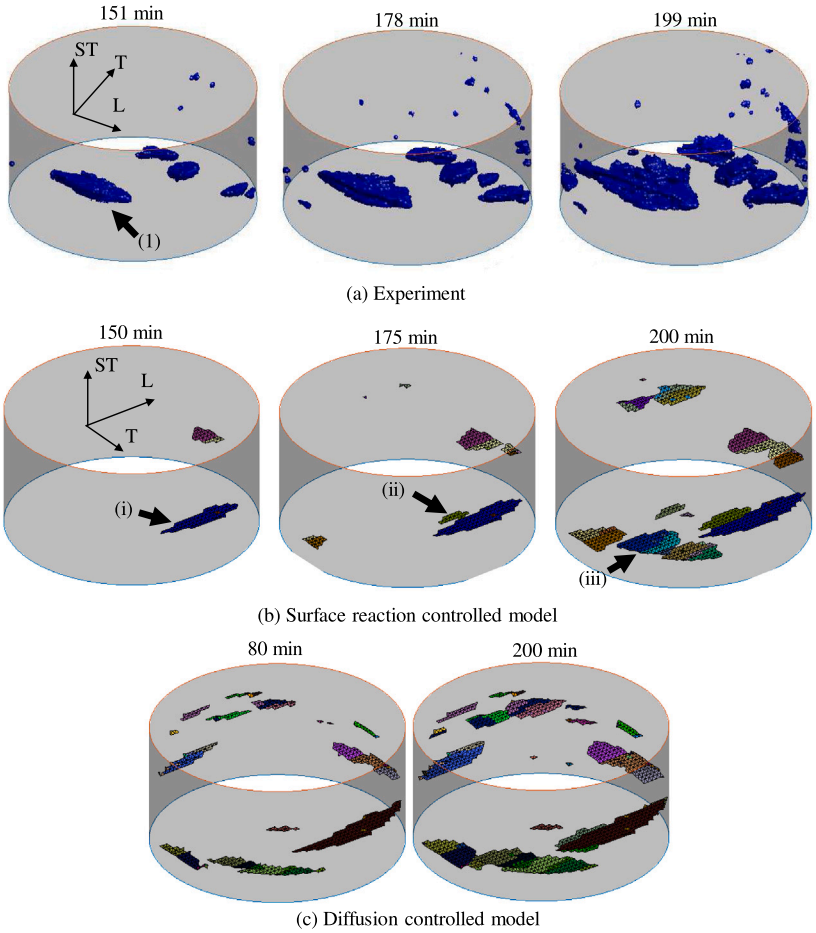


**Fig. 12.** The 3D crack growth behaviour observed (a) experimentally, (b) in the surface-reaction controlled model and (c) the diffusion controlled model. The snapshots have been labelled with the exposure time. The cracks in the model have been filled with different colours to indicate different grain boundaries. The outline of the sample surface has been shaded for clarity.

## 7. Discussion

### *7.1. Synthetic microstructures for probabilistic assessments*

From Fig. 16, the cracking behaviour of ten randomly generated synthetic microstructures with identical grain size/shape statistics were found to fracture at different rates. Experimentally, HEAC samples with nominally similar material properties subjected to equivalent loading and environmental conditions also exhibit some form of statistical variability in the fracture behaviour. For example, for smooth static tensile samples of AA7449-T7651 loaded at 100 MPa in moist air, the time to failure of three samples ranged between 160 and 287 days [37]. This is due to the stochastic nature of the material, loading parameters and the environment [54]. For example, the distribution and size of the grains at the gauge section is unique for each individual sample, despite having similar statistics. This is especially true for small samples, where a large grain size can cause a large variability in the microstructure of each sample. Thus, it is necessary to perform probabilistic assessments (both experimentally and for modelling, where the microstructure is incorporated) to accurately evaluate the cracking lifetime of components. Though aircraft structures and engineering components are usually much larger than the samples tested in this investigation, cracking often initiates at localised stress concentrators or other strain mismatch features (e.g. second phase particles) [55]. Therefore, the microstructure surrounding these concentrators can also vary randomly from one to another. Thus, if the grain size statistics of the material can be estimated accurately, generating random synthetic microstructures could be useful to perform Monte Carlo simulations to assess the variability in the HEAC behaviour for a specific component geometry. Given the apparent sensitivity of cracking to the microstructure, care is needed to design experimental samples of appropriate size. Samples that are small compared to the stressed component may exhibit excessive scatter. Samples that are too large may suggest a level of predictability that is not warranted.

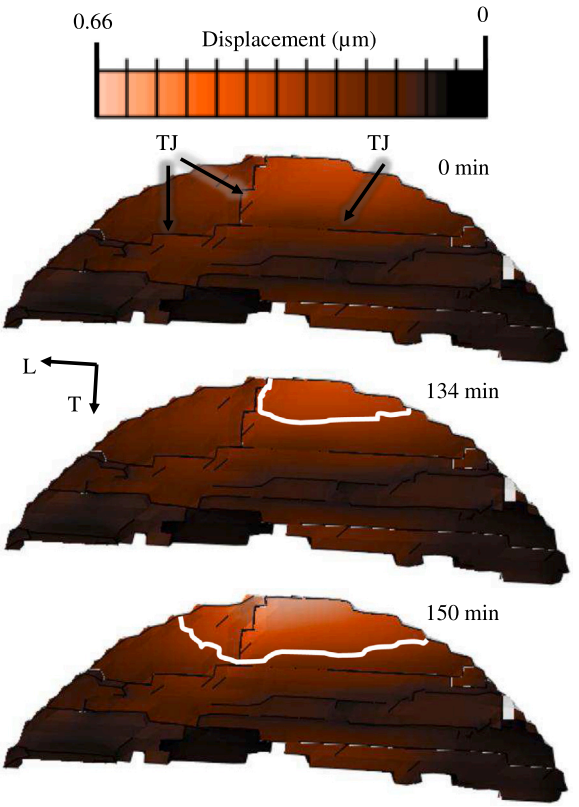


**Fig. 13.** Snapshots of the grain boundaries along which the crack labelled as (i) in Fig. 12(b) propagated, for exposure times of 0, 134 and 150 min. The grain boundaries have been coloured to show the contours for the opening displacement of the cohesive surfaces. Some triple junctions (TJ) have been labelled. The white lines represent the outline of crack (i).

### *7.2. Further developments*

The model developed was found to plausibly mimic the crack growth behaviour of AA7449-T7651. However, the model was simplified by applying several assumptions such as ignoring the hydrogen trapping behaviour at defects. This section discusses how the model can be evolved by adding complexity to the surface-reaction boundary conditions and the microstructural mesh.

#### *7.2.1. Surface-reaction kinetics*

For the surface-reaction controlled case, the hydrogen influx at the sample surface and cracked surfaces was assumed to be constant. However, the reaction rates at the surface are not typically constant. For example, the exposure of aluminium to water vapour results in the growth of the oxide film at the surface [56]. In this case, the reaction rates at the surface are dominated by inverse logarithmic kinetics [56]. This can be implemented by using an exponential decay amplitude curve for the boundary conditions in Abaqus:

$$q = Q_0 + Q\exp(-t/t_d), \tag{11}$$

where $q$ is the hydrogen flux at the surface, $Q_0$ is the initial flux, $Q$ is a coefficient and $t_d$ is the decay time. The use of a constant hydrogen flux for the surface-reaction controlled case gave similar quantitative and qualitative crack growth behaviour to the experimental results. Therefore, the use of an exponential decay curve was not necessary for the boundary conditions. There is insufficient data regarding the surface-reaction kinetics, however, it is possible that the decay time in moist air conditions is very large. Thus, the use of a decay function might not be necessary for samples subjected to short exposure times (e.g. the in-situ tensile samples from the case study).

It was not possible to differentiate between cohesive surfaces belonging to external cracks or internal cracks that had not surfaced in the UINTER subroutine (cohesive surfaces). Therefore, hydrogen was assumed to enter the sample at all fracture surfaces rather than just those exposed to the environment. This had a negligible influence for the diffusion controlled model, where only one crack was found to form internally. For the surface-reaction limited case, cracks also formed mostly at the sample surface. Therefore, the artificial hydrogen influx at internal cracks was not significant relative to the total hydrogen influx. Additionally, the high diffusivity resulted in an almost homogeneous hydrogen concentration throughout the sample, regardless of the source of hydrogen. Therefore,

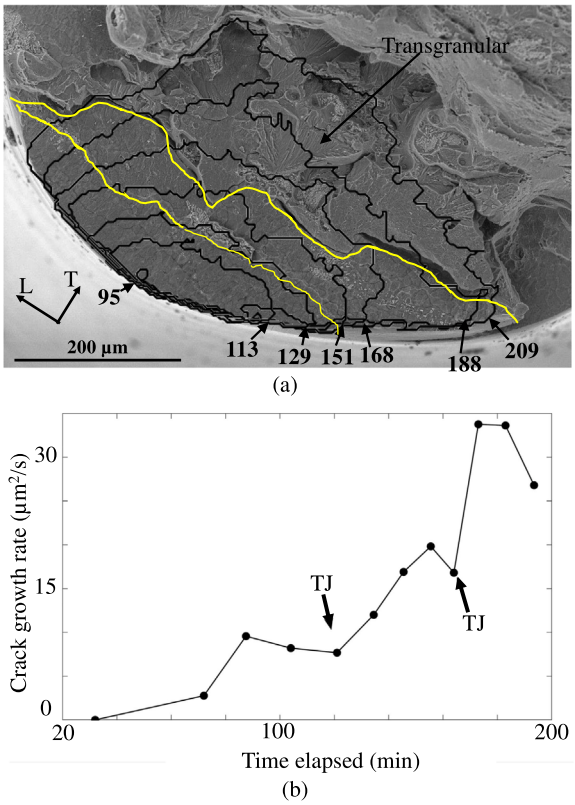


**Fig. 14.** (a) SEM fractograph of crack (1) in Fig. 12. The black lines show the outline of the crack after different exposure times. The labels indicate the exposure time in minutes. The yellow lines correspond to grain boundary triple junctions. (b) Graph showing the crack growth rate of crack (1) over time. The dips in the crack growth at which the crack reached the triple junctions emphasised in (a) have been labelled as 'TJ'.

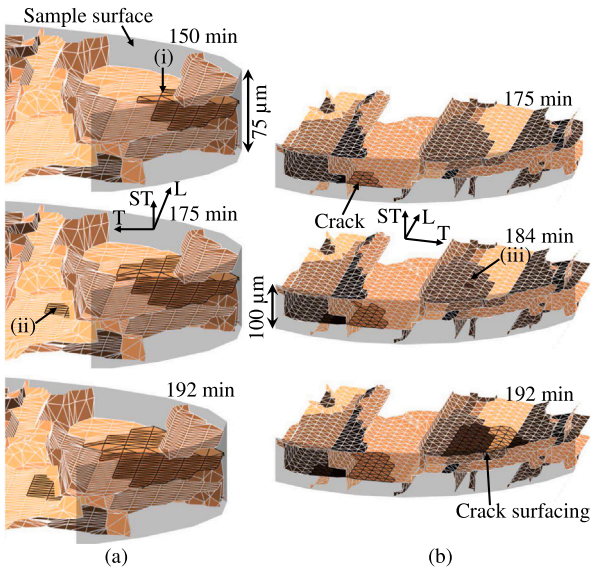


**Fig. 15.** Close-up images of the grain boundaries surrounding the cracks labelled (i)–(iii) in Fig. 12(b). The snapshots have been labelled with the exposure time. The faces of the cohesive surfaces belonging to different grain boundaries have been filled with different colours for clarity. The edges of the cohesive surface mesh are shown in white and the edges of the fractured surfaces are shown in black.

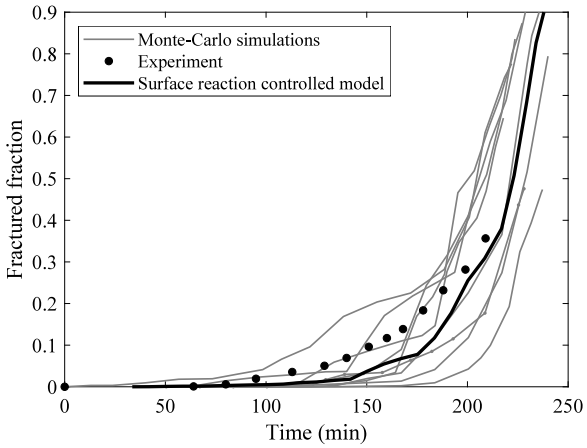


**Fig. 16.** The evolution of the fractured fraction for ten random synthetic microstructures using the same grain size/shape statistics in Dream.3D. The dark line represents the microstructure in Fig. 3.

the morphological HEAC behaviour was not affected by this issue. However, this issue must be addressed for accurate: (a) diffusion limited models with internal cracks, (b) any models with a significant fraction of internal cracks and (c) models with internal cracks and non-isotropic hydrogen diffusion.

*7.2.2. Grain boundary engineering and secondary phases*

The model implemented was based on the assumption that the cohesive properties of all of the high angle grain boundaries were identical. However, 7xxx aluminium alloys, including AA7449-T7651, contain a mixture of recrystallised and un-recrystallised grains [37]. Previous research indicates that the grain boundaries at the interface of recrystallised grains could be more sensitive to HEAC [15]. Similarly, some special grain boundaries are known to be less sensitive to intergranular stress corrosion cracking for austenitic stainless steels [57]. Therefore, more accurate environmentally assisted cracking models require a mixture of cohesive T–S parameters to account for the variable sensitivity of different grain boundaries. Furthermore, crack nucleation has often been correlated with the cracking of constituent particles or particle–matrix interfaces [15]. Additionally, these can also block the growth of existing cracks and cause crack arrest [15]. Constituent particles could also be incorporated to more complex models to enable further micro-mechanisms for crack growth and arrest. Cohesive modelling has previously been implemented to model particle cracking [58]. However, this would considerably increase the number of parameters required for calibration and increase the complexity of the model. Further, such a model would demand accurate data on particle distribution that simply may not be available.

## 8. Conclusion

In this work, a microstructure-sensitive cohesive zone model for HEAC has been developed and implemented. The process encompasses the generation of a random synthetic microstructure with Dream.3D, as well as the use of a coupled stress-diffusion analysis in Abaqus. The model was implemented to mimic the HEAC behaviour during crack initiation and microstructurally short cracking of AA7449-T7651 in moist air. The results found the following:

i. The influence of the orientation of grain boundaries relative to the tensile loading axis on the local crack growth rates and sensitivity to cracking was successfully accounted for by limiting the damage initiation and fracture criteria to the normal axes of the cohesive surfaces.
ii. Cracks were found to slow down at grain boundary triple junctions, as seen in real samples.
iii. Two different scenarios were modelled, including surface-reaction and diffusion controlled HEAC. It was inferred from the crack growth rates and qualitative comparisons that the HEAC rates of the real samples were likely limited by the influx of hydrogen at the surface rather than the diffusion coefficient.
iv. Randomly generated microstructures, exposed to identical circumstances, demonstrated variability in cracking behaviour. This emphasises the importance of developing models that incorporate microstructure for cracking phenomena operating on this length scale.

## Declaration of competing interest

The authors declare that they have no known competing financial interests or personal relationships that could have appeared to influence the work reported in this paper.

## Data availability

The files used to obtain the results are available online, including:

i. 1mm_diameter_cylinder.json: The pipeline used to generate the synthetic microstructure in Dream3D.

ii. gmsh.inp: The Abaqus file output by the Dream3D pipeline.

iii. Surface_Optimised_C3D4T_bcp3: The MATLAB code used to generate the required Abaqus input file with defined material properties, cohesive surfaces and loading/boundary conditions.

iv. Input_file.inp: The Abaqus input file for the final model results presented in Figures 7–15.

v. KUINTER_surf_crack_outer10.for : The user subroutine used for the final model. The subroutine encompasses the constitutive mechanical and diffusion behaviour of the grains (C3D4T elements) and the grain boundaries (cohesive surfaces).

## Acknowledgements

Funding was provided by the Engineering and Physical Sciences Research Council (EPSRC), United Kingdom in a doctoral training partnership for a PhD at the University of Bristol. We would like to thank Mike Jackson from BlueQuartz software for his support for the Dream.3D pipeline. Additionally, we would like to thank Dr Antonio Melro for his suggestions during the development of the Abaqus subroutine. We would also like to acknowledge the advanced computing research centre at the University of Bristol for providing access to the BlueCrystal Phase 3 supercomputer.

## References

[1] Oriani R. Hydrogen embrittlement of steels. Annu Rev Mater Sci 1978;8(1):327–57.
[2] Tal-Gutelmacher E, Eliezer D. The hydrogen embrittlement of titanium-based alloys. Jom 2005;57(9):46–9.
[3] Speidel MO, Hyatt MV. Stress-corrosion cracking of high-strength aluminum alloys. In: Advances in corrosion science and technology. Springer; 1972, p. 115–335.
[4] Gangloff R. Hydrogen-assisted cracking. comprehensive structural integrity, volume 6: environmentally-assisted fracture. Oxford: Elsevier; 2003.
[5] Kholtobina AS, Ecker W, Pippan R, Razumovskiy VI. Effect of alloying elements on hydrogen enhanced decohesion in bcc iron. Comput Mater Sci 2021;188:110215.
[6] Birnbaum HK, Sofronis P. Hydrogen-enhanced localized plasticity—a mechanism for hydrogen-related fracture. Mater Sci Eng A 1994;176(1–2):191–202.
[7] Lynch S. A fractographic study of hydrogen-assisted cracking and liquid-metal embrittlement in nickel. J Mater Sci 1986;21(2):692–704.
[8] Griesche A, Dabah E, Kannengiesser T, Kardjilov N, Hilger A, Manke I. Three-dimensional imaging of hydrogen blister in iron with neutron tomography. Acta Mater 2014;78:14–22.
[9] Young GA, Scully JR. Hydrogen production, absorption and transport during environment assisted cracking of an al-zn-mg-(cu) alloy in humid air. In: Hydrogen effects on material behavior and corrosion deformation interactions. Warrendale, OH, USA: TMS; 2003, p. 893–907.
[10] Yang L, He L, Huang D, Wang Y, Song Q, Zhao L, Shen X, Tian Z, Wang H. Three-dimensional hydrogen distribution and quantitative determination of titanium alloys via neutron tomography. Analyst 2020;145(12):4156–63.
[11] Boellinghaus T, Hoffmeister H. Numerical model for hydrogen-assisted cracking. Corrosion 2000;56(6):611–22.
[12] Martínez-Pañeda E, Niordson CF, Gangloff RP. Strain gradient plasticity-based modeling of hydrogen environment assisted cracking. Acta Mater 2016;117:321–32.
[13] Mandal TK, Nguyen VP, Wu J-Y. Comparative study of phase-field damage models for hydrogen assisted cracking. Theor Appl Fract Mech 2021;111:102840.
[14] Gudla VC, Storm M, Palmer BC, Lewandowski JJ, Withers PJ, Holroyd NH, Burnett TL. Environmentally induced crack (eic) initiation, propagation, and failure: A 3d in-situ time-lapse study of aa5083 h131. Corros Sci 2020;174:108834.
[15] De Francisco U, Larrosa NO, Peel MJ. Hydrogen environmentally assisted cracking during static loading of aa7075 and aa7449. Mater Sci Eng A 2020;772:138662.
[16] Kalbert S, Ramasubbu V, Parvathavarthini N, Gill TP. Influence of alloying on hydrogen-assisted cracking and diffusible hydrogen content in cr-mo steel welds. Sadhana 2003;28(3–4):383–93.
[17] Lessar J, Gerberich WW. Grain size effects in hydrogen-assisted cracking. Metall Trans A 1976;7(7):953–60.
[18] Chou S-L, Tsai W-T. Effect of grain size on the hydrogen-assisted cracking in duplex stainless steels. Mater Sci Eng A 1999;270(2):219–24.
[19] Jivkov AP, Stevens NP, Marrow TJ. Mesoscale mechanical model for intergranular stress corrosion cracking and implications for microstructure engineering. J Press Vessel Technol 2008;130(3).
[20] McDowell D, Dunne F. Microstructure-sensitive computational modeling of fatigue crack formation. Int J Fatigue 2010;32(9):1521–42.
[21] Arafin M, Szpunar J. A novel microstructure–grain boundary character based integrated modeling approach of intergranular stress corrosion crack propagation in polycrystalline materials. Comput Mater Sci 2010;47(4):890–900.
[22] Ayyar A, Chawla N. Microstructure-based modeling of crack growth in particle reinforced composites. Compos Sci Technol 2006;66(13):1980–94.
[23] Zhang J, Ouyang Q, Guo Q, Li Z, Fan G, Su Y, Jiang L, Lavernia EJ, Schoenung JM, Zhang D. 3D microstructure-based finite element modeling of deformation and fracture of sicp/al composites. Compos Sci Technol 2016;123:1–9.
[24] Martínez-Pañeda E, Golahmar A, Niordson CF. A phase field formulation for hydrogen assisted cracking. Comput Methods Appl Mech Engrg 2018;342:742–61.
[25] Lee GH, Shim JS, Cui CY, Beom HG. Hydrogen-induced cracking of an aluminum single crystal: An atomistic simulation. Comput Mater Sci 2019;169:109084.
[26] Jeon J-Y, Larrosa NO, Oh Y-R, Kim Y-J, Ainsworth RA. Characterization of the effect of notch bluntness on hydrogen embrittlement and fracture behavior using fe analyses. In: Pressure vessels and piping conference, Vol. 56994. American Society of Mechanical Engineers; 2015, V06AT06A021.
[27] Falkenberg R, Brocks W, Dietzel W, Schneider I. Simulation of stress-corrosion cracking by the cohesive model. In: Key engineering materials, Vol. 417. Trans Tech Publ; 2010, p. 329–32.
[28] Brocks W, Falkenberg R, Scheider I. Coupling aspects in the simulation of hydrogen-induced stress-corrosion cracking. Proc Iutam 2012;3:11–24.
[29] Alvaro A, Olden V, Akselsen OM. 3D cohesive modelling of hydrogen embrittlement in the heat affected zone of an x70 pipeline steel–part ii. Int J Hydrogen Energy 2014;39(7):3528–41.
[30] Jemblie L, Olden V, Akselsen OM. A review of cohesive zone modelling as an approach for numerically assessing hydrogen embrittlement of steel structures. Phil Trans R Soc A 2017;375(2098):20160411.
[31] Jemblie L, Olden V, Mainçon P, Akselsen OM. Cohesive zone modelling of hydrogen induced cracking on the interface of clad steel pipes. Int J Hydrogen Energy 2017;42(47):28622–34.

[32] Yu H, Olsen JS, Olden V, Alvaro A, He J, Zhang Z. Viscous regularization for cohesive zone modeling under constant displacement: An application to hydrogen embrittlement simulation. Eng Fract Mech 2016;166:23–42.
[33] Gao Y, Li B, Wang J, Feng X-Q. Fracture toughness analysis of helical fiber-reinforced biocomposites. J Mech Phys Solids 2021;146:104206.
[34] Simonovski I, Cizelj L. Towards modeling intergranular stress corrosion cracks on grain size scales. Nucl Eng Des 2012;246:107–14.
[35] Simonovski I, Cizelj L. Cohesive element approach to grain level modelling of intergranular cracking. Eng Fract Mech 2013;110:364–77.
[36] Simonovski I, Cizelj L. Cohesive zone modeling of intergranular cracking in polycrystalline aggregates. Nucl Eng Des 2015;283:139–47.
[37] Schwarzenböck E, Ollivier E, Garner A, Cassell A, Hack T, Barrett Z, Engel C, Burnett TL, Holroyd NH, Robson JD, et al. Environmental cracking performance of new generation thick plate 7000-t7x series alloys in humid air. Corros Sci 2020;171:108701.
[38] De Francisco U, Beckmann F, Moosmann J, Larrosa NO, Peel MJ. 3D characterisation of hydrogen environmentally assisted cracking during static loading of AA7449-T7651. Int J Fract 2021;232(1):93–116.
[39] Groeber MA, Jackson MA. Dream. 3d: a digital representation environment for the analysis of microstructure in 3d. Integr Mater Manuf Innov 2014;3(1):5.
[40] BlueQuartz. Statsgenerator. 2020, http://www.dream3d.io/Filters/SyntheticBuildingFilters/StatsGeneratorFilter/ (Accessed: 11/01/2021).
[41] Geuzaine C, Remacle J-F. Gmsh: A 3-d finite element mesh generator with built-in pre-and post-processing facilities. Internat J Numer Methods Engrg 2009;79(11):1309–31.
[42] Oh C-S, Kim Y-J, Yoon K-B. Coupled analysis of hydrogen transport using abaqus. J Solid Mech Mater Eng 2010;4(7):908–17.
[43] Barrera O, Tarleton E, Tang H, Cocks A. Modelling the coupling between hydrogen diffusion and the mechanical behaviour of metals. Comput Mater Sci 2016;122:219–28.
[44] MatWeb. Aluminum 7075-t6; 7075-t651. 2021, http://www.matweb.com/search/DataSheet.aspx?MatGUID=4f19a42be94546b686bbf43f79c51b7d (Accessed: 25/03/2021).
[45] Young GA, Scully JR. Hydrogen production, absorption and transport during environment assisted cracking of an al-zn-mg-(cu) alloy in humid air. In: Moody N, editor. Int. conf. on hydrogen effects on material behavior and corrosion deformation interactions. Warrendale, PA: The Minerals, Metals, and Materials Society; 2002, p. 893.
[46] Systemes D. Abaqus analysis user's guide, version 6.14. Providence, RI, USA: Dassault Systemes Simulia Corp.; 2014.
[47] Katzarov IH, Paxton AT. Hydrogen embrittlement ii. Analysis of hydrogen-enhanced decohesion across (111) planes in $\alpha$-fe. Phys Rev Mater 2017;1(3):033603.
[48] Jemblie L, Olden V, Akselsen OM. A coupled diffusion and cohesive zone modelling approach for numerically assessing hydrogen embrittlement of steel structures. Int J Hydrogen Energy 2017;42(16):11980–95.
[49] Scheider I, Pfuff M, Dietzel W. Simulation of hydrogen assisted stress corrosion cracking using the cohesive model. Eng Fract Mech 2008;75(15):4283–91.
[50] Pu C, Gao Y, Wang Y, Sham T-L. Diffusion-coupled cohesive interface simulations of stress corrosion intergranular cracking in polycrystalline materials. Acta Mater 2017;136:21–31.
[51] Wei R, Simmons G. Recent progress in understanding environment assisted fatigue crack growth. Int J Fract 1981;17(2):235–47.
[52] Wei RP. Fracture mechanics: integration of mechanics, materials science and chemistry. Cambridge University Press; 2010.
[53] Burnett TL, Holroyd NH, Scamans GM, Zhou X, Thompson GE, Withers PJ. The role of crack branching in stress corrosion cracking of aluminium alloys. Corros Rev 2015;33(6):443–54.
[54] Zentuti N, Booker J, Hoole J, Bradford R, Knowles D. Probabilistic structural integrity. In *Proceedings of the tagsi-fesi symposium on probabilistics*, 2018.
[55] Lynch S. Failures of structures and components by envirnomentally assisted cracking. Eng Fail Anal 1994;1(2):77–90.
[56] Do T, Splinter S, Chen C, McIntyre N. The oxidation kinetics of mg and al surfaces studied by aes and xps. Surf Sci 1997;387(1–3):192–8.
[57] King A, Johnson G, Engelberg D, Ludwig W, Marrow J. Observations of intergranular stress corrosion cracking in a grain-mapped polycrystal. Science 2008;321(5887):382–5.
[58] Steglich D, Siegmund T, Brocks W. Micromechanical modeling of damage due to particle cracking in reinforced metals. Comput Mater Sci 1999;16(1–4):404–13.